

# Highly Efficient In Vivo Cancer Therapy by an Implantable Magnet Triboelectric Nanogenerator

Chaochao Zhao, Hongqing Feng, Lijun Zhang, Zhe Li, Yang Zou, Puchuan Tan, Han Ouyang, Dongjie Jiang, Min Yu, Chan Wang, Hu Li, Lingling Xu, Wei Wei,\* and Zhou Li\*

In this work, a nanogenerator-controlled drug delivery system (DDS) for use in cancer therapy is successfully established. A new magnet triboelectric nanogenerator (MTENG) is fabricated that can guarantee the contact and detach cycle between the two friction layers and effectively increase the TENG output, up to 70 V after implantation. Using a special structural design, without the commonly used spacer, this contacting-mode MTENG can ensure a high and consistent electricity output after encapsulation and implantation. Doxorubicin-(DOX-) loaded red blood cells (RBCs) are employed as the anti-tumor DDS in this study. After DOX loading, the RBC membranes are stable and the self-release is very slow. However, upon electric stimulation from the MTENG, the release of DOX is remarkably increased, and falls back to normal again after the stimulation. Thus a controllable DDS is established. The MTENG-controllable DDS achieves an outstanding killing of carcinomatous cells both in vitro and in vivo at a low DOX dosage. These results demonstrate a prominent therapeutic effect of the MTENG-controlled DDS for cancer therapy, which is highly promising for application in the clinic.

## 1. Introduction

Chemotherapy for cancers has been well known to have severe side effects and low therapeutic efficacy. For example, Doxorubicin (DOX), one of the most famous chemotherapeutic drugs, is frequently used in the treatment of various solid and hematopoietic tumors.<sup>[1]</sup> Meanwhile, DOX has been reported to cause many toxic side effects, including cardiotoxicity, myelosuppression, mucositis, and alopecia.<sup>[2]</sup> To overcome the shortcomings of the chemotherapeutic drugs, targeted drug delivery systems (DDS) have been proposed and extensively studied in the past few decades.<sup>[3]</sup> DDS are designed to improve the specific targeting, increase drug delivery to the sites of interest, and decrease the incidence and intensity of the side effects.

Among these efforts, nanoscaled particles and vehicles have attracted great interest because of the enhanced permeation and retention (EPR) effect for tumors.<sup>[4]</sup> To date, many nanovehicles have been developed, such as micelles,<sup>[5]</sup> nanoparticles,<sup>[6]</sup> microcapsules,<sup>[7]</sup> and nanogels.<sup>[8]</sup> However, few of them have fully met the clinical requirements due to their biotoxicity and unsatisfactory pharmacokinetic index. Most recently, cell or cell-derived membrane vehicle based DDS have attracted much attention by virtue of their biological origin, intrinsic biocompatibility, and a variety of physicochemical properties.<sup>[9]</sup> Among them, red blood cells (RBCs) are good candidates because they have perfect biocompatibility, no immunogenicity as autograft, easy availability, long circulating half-life (120 d in humans), and membrane flexibility and stability.<sup>[10]</sup> Although RBCs have a diameter of micrometers, they are still within the effective size range of EPR (300 nm–4.7 μm).<sup>[11]</sup> In addition, their membrane flexibility allows them to permeate to the tumor sites. With the help of magnet nanoparticles and surface ligates, the permeation and localization efficiency can become even higher.<sup>[12]</sup>

DDS are committed to reduce the drug release in unwanted sites but to enhance it in the targeted sites. Therefore stimulative or controllable release behavior is a preferred feature. RBC-based DDS that can be responsive to stimulations such as electric field (EF), near-infrared light, magnetic field, and ultrasound have been established.<sup>[13]</sup> Among the aforementioned external stimulations, EF is regarded as an attractive

C. C. Zhao, Dr. H. Q. Feng, Z. Li, Y. Zou, P. C. Tan, H. Ouyang,  
D. J. Jiang, M. Yu, C. Wang, H. Li, L. L. Xu, Prof. Z. Li  
CAS Center for Excellence in Nanoscience  
Beijing Key Laboratory of Micro-nano Energy and Sensor  
Beijing Institute of Nanoenergy and Nanosystems  
Chinese Academy of Sciences  
Beijing 100083, P. R. China  
E-mail: zli@binn.cas.cn

C. C. Zhao, Dr. H. Q. Feng, Z. Li, Y. Zou, P. C. Tan, H. Ouyang,  
D. J. Jiang, M. Yu, C. Wang, H. Li, L. L. Xu, Prof. Z. Li  
School of Nanoscience and Technology  
University of Chinese Academy of Sciences  
Beijing 100049, P. R. China

L. J. Zhang, Prof. W. Wei  
State Key Laboratory of Biochemical Engineering  
Institute of Process Engineering  
Chinese Academy of Sciences  
Beijing 100190, P. R. China  
E-mail: weiwei@ipe.ac.cn

Prof. Z. Li  
Center on Nanoenergy Research  
School of Physical Science and Technology  
Guangxi University  
Nanning 530004, P. R. China

 The ORCID identification number(s) for the author(s) of this article can be found under <https://doi.org/10.1002/adfm.201808640>.

DOI: 10.1002/adfm.201808640

choice because of its minimal invasiveness, the ability to reach targeted tissues, easy manipulation, and low cost.<sup>[14]</sup> However, traditional EF source is generated by commercial high voltage power supply with bulk volume and insecurity, which holds back its application as a portable or wearable device. Moreover, depletion of energy source is also a severe challenge for its medical application.

Recently, the development of nanogenerators as self-powered energy sources has gained tremendous progresses.<sup>[15]</sup> Triboelectric nanogenerators (TENGs) can be easily fabricated and miniaturized using flexible materials, and generate voltages up to kilovolt from unordered ambient mechanical energy.<sup>[16]</sup> TENGs have been successfully applied as wearable power source to harvest the energy from body motions.<sup>[17]</sup> Several frontier researchers have also proved the feasibility of developing TENG-based implantable biomedical devices.<sup>[18]</sup> Therefore implantable TENGs can be a promising solution toward EF-controlled DDS with its small scale and infinite energy supply.

In this article, we demonstrated the first TENG supported controllable DDS for cancer therapy and obtained an outstanding anti-tumor efficacy *in vivo*. An encapsulated magnet-TENG (MTENG) with novel structure was fabricated to control the drug release from the DOX loaded RBCs (D@RBCs). Under the EF stimulation by the MTENG, the DOX release was significantly increased; after the EF withdrawal, the release went back to normal again. Thus the MTENG resulted in a controllable drug release pattern. The MTENG supported DDS not only induced great viability reduction in traditional 2D culture of HeLa cells but also prompted significant growth inhibition and cell apoptosis in the 3D multicellular spheroids (MCTS). In further, the TENG enhanced DDS were applied in tumor-bearing nude mice and demonstrated an excellent anti-tumor efficacy *in vivo*.

## 2. Result and Discussion

### 2.1. Fabrication and Characteristics of the MTENG

**Figure 1A,B** illustrates the detailed structure of the MTENG. Polytetrafluoro ethylene (PTFE) and titanium were used as the two friction layers. Nanostructures were made on the PTFE surface to enhance the output of the MTENG. A Cu film with a thickness of 200 nm was magnetron sputtered on the back of PTFE to act as an electrode. The outer PTFE and polydimethylsiloxane (PDMS) film served as encapsulation layers to protect the MTENG from harsh environment. The diameter of the friction layers and the encapsulation layers was 2.5 and 4 cm, respectively. Early reported TENGs usually have spacer structure or “keel structure,”<sup>[19]</sup> but one main challenge is that after the TENG is encapsulated or works for a long time, the output will decrease significantly because the two friction layers have less tendency to detach from each other gradually. To overcome this challenge, we designed this MTENG employing a pair of small magnets. Two magnets with a diameter of 8 mm were fixed on the back of the two friction layers to separate them via magnetic repulsion (**Figure 1C**). Detailed working principle based on the coupling of contact electrification and electrostatic induction of the MTENG is illustrated in **Figure 1D**. Electrons

are driven back and forth through the external circuit under a periodic mechanical force. Before encapsulation, the open-circuit voltage ( $V_{oc}$ ), short-circuit current ( $I_{sc}$ ), and transferred charge ( $Q_{sc}$ ) could reach 70 V, 0.55  $\mu$ A, and 25 nC, respectively (**Figure 1E**, and **Figure S1A,D**, Supporting Information). After encapsulation and implantation subcutaneously in stinky pork, the  $V_{oc}$ ,  $I_{sc}$ , and  $Q_{sc}$  were just the same as the pre-encapsulation ones (**Figure 1F,G**, and **Figure S1B,C,E,F**, Supporting Information). This advantage resulted from the magnets, which effectively guaranteed the contact and separation process of the MTENG. The MTENG also exhibited very long life cycle; the outputs were the same as the initial state after 100 000 cycles (**Figure S2**, Supporting Information). These results all suggested that our MTENGs were very suitable to serve as implantable power source for medical applications.

### 2.2. DOX Loading into RBCs

The hypotonic dialysis method was used to load DOX into RBCs in this experiment. Briefly, a mix of fresh RBC suspension and DOX with a concentration of 200  $\mu$ g mL<sup>-1</sup> (**Figure S3**, Supporting Information) was incubated at 4 °C, and then the inflated RBCs were transferred into a hypertonic buffer at 37 °C to recover the osmotic pressure and reseal the membranes. Glutathione (GSH), adenosine triphosphate (ATP), and some other metabolic stabilizer were added during the loading step to protect the RBCs from oxidative damage and protect the membrane structure.

Almost all the RBCs were kept intact after drug loading and stored for 7 d (**Figure S4A,B**, Supporting Information). Obvious DOX fluorescence was observed in the confocal images, suggesting that DOX had been successfully encapsulated inside the RBCs (**Figure 2A**). The fluorescence emission spectra further confirmed the D@RBCs had the same emission peak as DOX at around 590 nm, while control RBCs had barely any fluorescence emission (**Figure S4C**, Supporting Information). Flow cytometry data (**Figure S4D,E**, Supporting Information) showed that about 90.0% of the D@RBCs were loaded with DOX. From the standard curve (**Figure S5**, Supporting Information) quantified by fluorescence emission spectra (DOX fluorescence), it was estimated that about 144  $\mu$ g DOX was loaded inside 1 mL RBC solution; in other words, about  $7.45 \times 10^7$  DOX molecules were loaded in each RBC on average. As for long-term release behaviors, above 70% of DOX was maintained in the RBC after 7 d, proving a low intrinsic DOX release kinetics (**Figure S4F**, Supporting Information).

### 2.3. Controlled Drug Release from D@RBCs by MTENG

After DOX loading, the EF generated by MTENG was applied on the D@RBCs in a 2D stimulation device. The device substrate was deposited with interdigital electrodes with widths of 100  $\mu$ m and gaps of 100  $\mu$ m. A layer of biocompatible PDMS of about 20  $\mu$ m thick was spin-coated on the electrodes for insulation. In order to protect RBC suspension from flow away, a biocompatible polylactic acid (PLA) mold made by 3D printing technology was fixed on the PDMS substrate to make

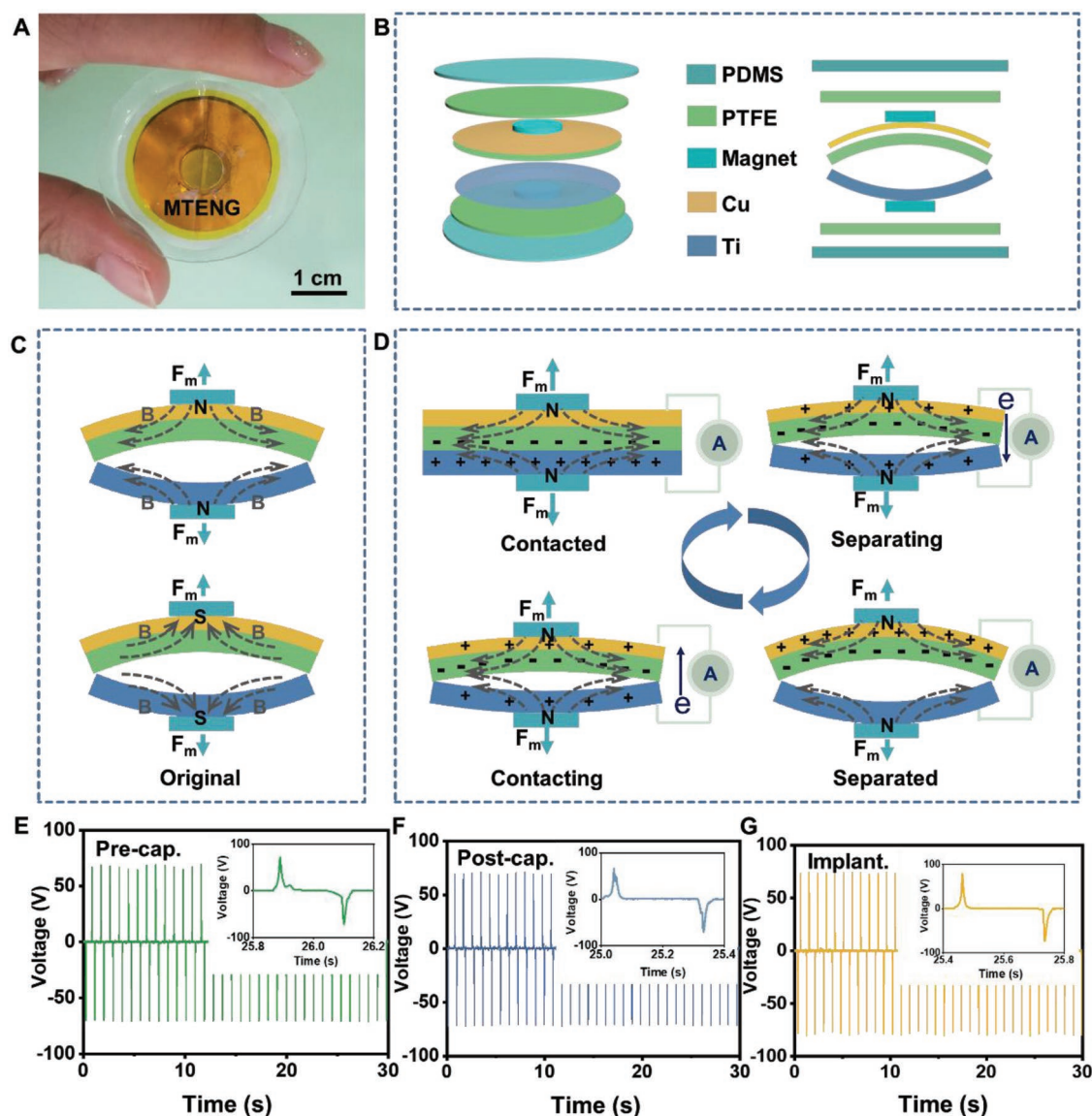


**Figure 1.** Device structure and output performance of the MTENG. A) Digital image and B) the schematic diagram of the MTENG. C) Original state of MTENG. The two friction layers separate from each other due to magnetic repulsion. D) Working principle of The MTENG. E, F)  $V_{oc}$  of the MTENG before and after encapsulation. G)  $V_{oc}$  of the MTENG after encapsulation and implanted subcutaneously in streaky pork.

a reservoir (Figure 2J). The output of the MTENG delivered to this device generated an EF up to  $4 \text{ kV cm}^{-1}$  (Figure 2B).

As shown in Figure 2C, after stimulated by the EF generated by MTENGs for 1 h, 40.3% of DOX was released from the RBCs. As time elapsed, the released DOX increased to 59.7% after 8 h of EF stimulation. In marked contrast, less than 14.4% of DOX was released in the same condition expect for the EF. Then the following experiment was carried out: the D@RBCs were treated with EF for 10 min, and the DOX release was monitored for 1 h (Figure 2D). The group with EF stimulation had much more DOX release than the group without EF at the end of 10 min EF treatment. When the MTENG stopped working, the EF group showed no difference of drug release with the control group during the next 20 and 50 min (Figure 2E). Figure 2E also shows that after being stimulated

by EF for 10 min, the released drug was more than threefold of the control; after being stimulated for 1 and 8 h, the release was about fourfold. These results demonstrated that the accelerated release of DOX only took place in the presence of EF.

To study the morphology changes in the membranes, scanning electron microscope (SEM) was employed before and after EF treatment. The initial RBCs (Figure 2F) and DOX loaded RBCs (Figure 2G) displayed normal biconcave shape, while the DOX loaded RBCs showed smaller diameter. After EF treatment for 10 min, some RBCs shrank and some exhibited obvious pores on the membrane (Figure 2H). These results demonstrated that electroporation had been induced in the RBC membranes by the EF. After the EF was withdrawn, the membrane pores healed by themselves (Figure 2I). Therefore the mechanisms of the TENG-controlled RBC DDS are illustrated in Figure 3J. Under

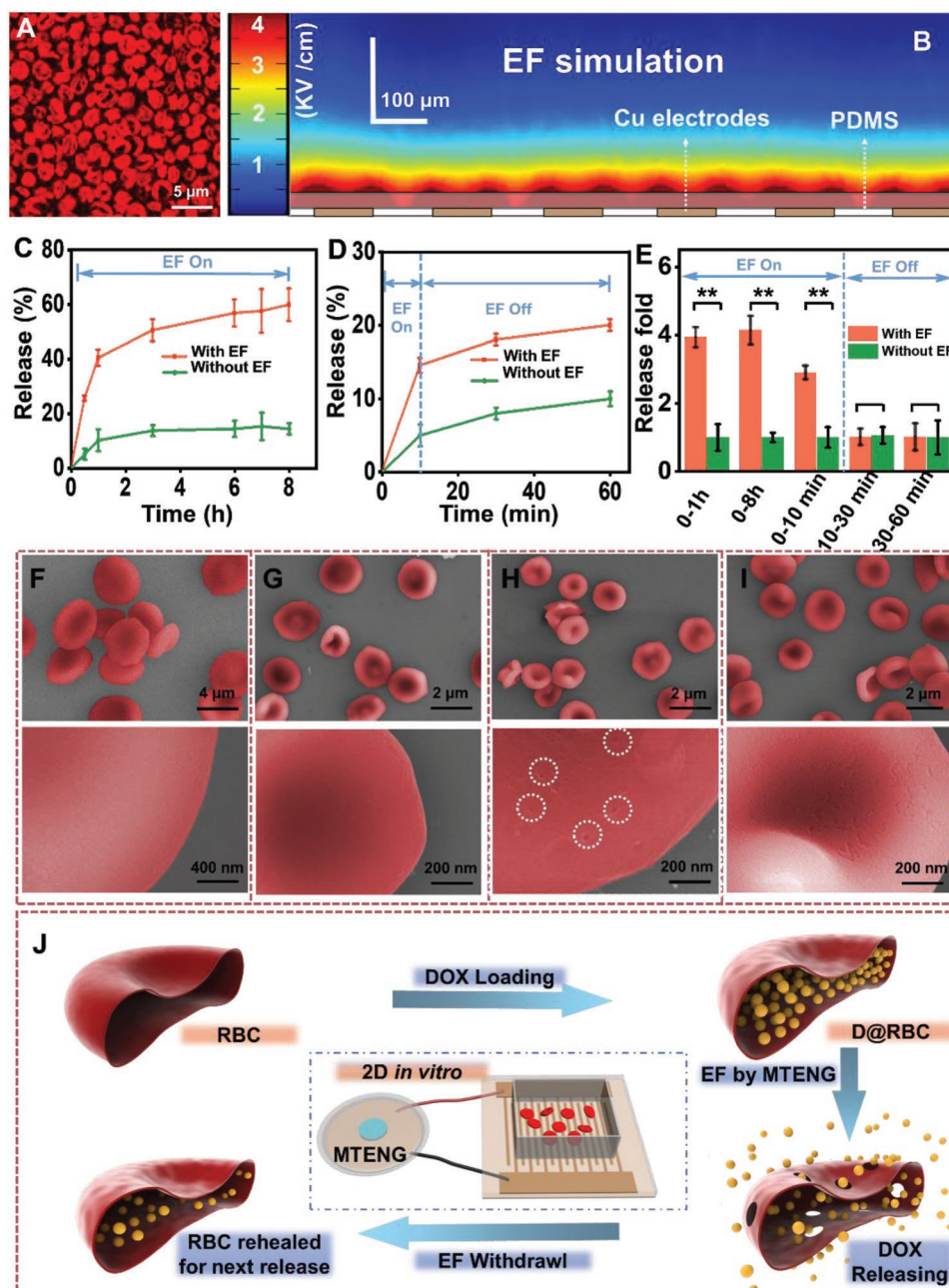


**Figure 2.** The MTENG-controlled release of D@RBCs. A) A confocal fluorescent image of D@RBCs. Red fluorescence suggested DOX had been successfully loaded into RBCs. B) Finite element analysis of the 2D stimulation device using COMSOL. C–E) Kinetics of MTENG-controlled drug release. The accelerated release of DOX only existed when the TENG generated electric pluses. F–I) SEM images of innate RBC, D@RBC, D@RBC+EF, and D@RBC after EF. J) Schematic illustration to show the loading of DOX into RBCs, and the subsequent integration of MTENG to realize controlled DOX release.

the high EF generated by TENG, nanopores were induced on the surface of RBCs. After the EF withdrawal, the pores could recover, resulting in a controlled DOX release.

#### 2.4. MTENG-Controlled RBC DDS to Treat 2D Cultured HeLa Cells

Next, the MTENG-controlled DDS was demonstrated in HeLa cells using the same stimulation device as in the measurement

of DOX release from D@RBCs. After the RBCs were added to the culture and stimulation device for about 30 min, they attached to the device substrate to have the same location as HeLa cells, which enabled an effective delivery of DOX to HeLa cells from the RBCs (Figure 3A). HeLa cell were incubated with RBCs, D@RBCs, or free DOX ( $0.1 \mu\text{g mL}^{-1}$ ), respectively, for half an hour, stimulated by the MTENGs for 1 h and further incubated for another 24 h. After that, CCK-8 assay was carried out to evaluate the cancer killing efficacy. The total amount of DOX in the free DOX group and the D@RBC group was carefully controlled to be the

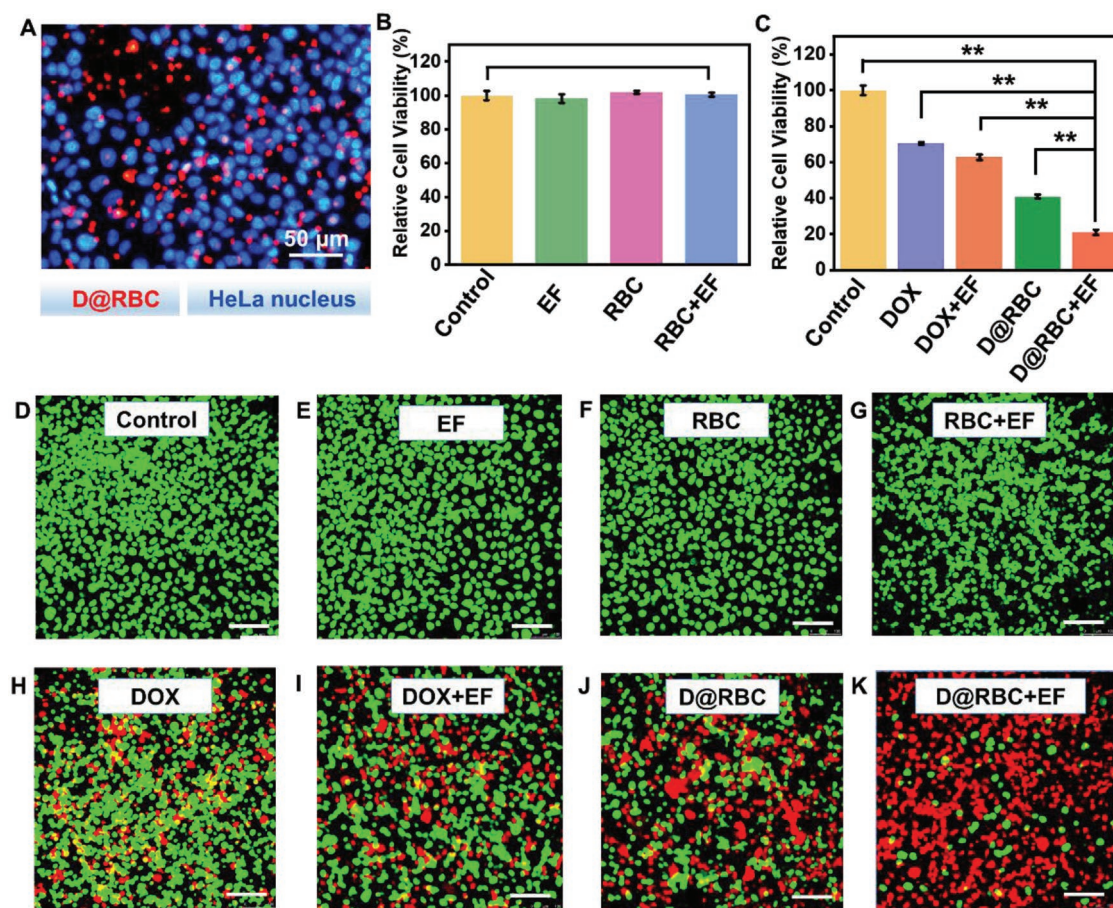


**Figure 3.** MTENG-controlled DDS to treat HeLa cells in 2D culture. A) The co-localization of the RBC and HeLa cells. B) The viabilities of HeLa cells in the control, EF, RBC, and RBC+EF groups were the same. C) The viabilities of HeLa cells in the DOX, DOX+EF, D@RBC, and D@RBC+EF groups decreased obviously. The data are shown as mean  $\pm$  SD. Error bars are based on at least triplicate measurements.  $p$  values:  $**p < 0.01$  or  $*p < 0.05$ . D–K) Live and dead analysis of HeLa cells in the different groups (scale bar: 50  $\mu$ m).

same. Untreated RBCs or EF stimulation, either individually or combined, had no influence on the cell survival (Figure 3B). Contrarily, the viability of HeLa cells treated with free DOX decreased to 70.4%, and those treated with free DOX+EF had a slightly improved therapeutic effect (viability decreased to 62.7%), probably because the EF increased the sensitivity of HeLa cells to DOX. The group of D@RBCs decreased the cell viability to 40.9%, demonstrating that the RBC DDS are more effective than free DOX therapy, because the localized release from the D@RBCs guaranteed a higher drug concentration at the bottom of the culture substrate where the cells also localized. Compared to the group of D@RBCs, an even higher cancer cell killing efficacy was observed in the group of D@RBC+EF (viability decreased to 20.9%). Live and dead analyses of HeLa cells are shown in Figure 3D–K, which were consistent with the viability assay. The above results demonstrated that our systems had significantly enhanced the killing of cancer cells in a 2D culture model.

## 2.5. MTENG-Controlled RBC DDS to Treat 3D MCTS

Traditional 2D cell culture model has been prevalently used to study the anti-tumor efficacy, but it also gives rise to the

concerns on its reliability to reflect the actual tumor development situations in vivo. Therefore, it is more convincing to investigate the anti-tumor efficiency of the EF-controlled DDS in a more advantaged evaluation system, the 3D MCTS culture system. The stimulation device is shown in Figure 4A and Figure S4 (Supporting Information). EF generated by the MTENG was delivered to the MCTS via two steel microneedles. The ends of the microneedles were insulated by a thin layer of parylene C. The distance between the two needle electrodes was about 400  $\mu$ m, and finite element analysis of COMSOL suggested EF up to 5  $\text{kV cm}^{-1}$  was generated around the needles (Figure 5A,B). An agarose culture method was used to support the growth of the 3D MCTS. After 4 d of culture, the MCTS grew into a diameter of about 400  $\mu$ m. Then the MCTS were incubated with the RBCs for 12 h, and the redundant RBCs were washed away later. The fluorescence microscopy images showed that RBCs (red) had successfully penetrated into the inside of the MCTS (blue) (Figure 4C–E). This situation was consistent with the EPR property of nanodrug carriers to tumors in vivo, which was very crucial for the following anti-tumor functions.

The anti-tumor efficiency of the MTENG-controlled RBC DDS was demonstrated by TUNEL assay and MCTS size

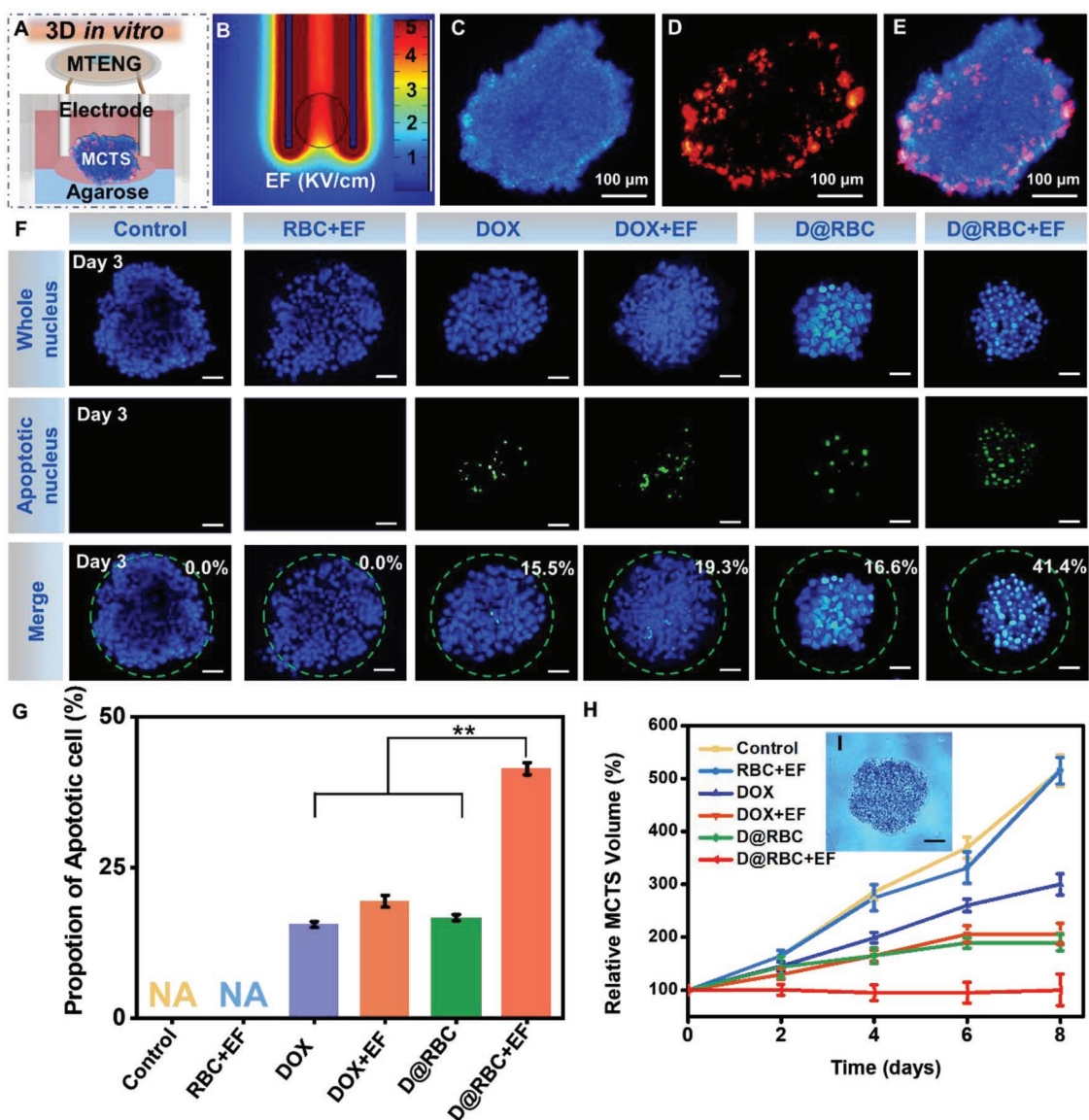


**Figure 4.** Evaluation of the antitumor ability of EF-controlled RBC DDS using the MCTS. A) Schematic diagram of 3D electroperoration device. B) Finite element analysis of 3D stimulation device by COMSOL. C–E) Colocalization of C) HeLa cells and D) RBCs. F) Representative fluorescent microscope images of TUNEL assay in cryosections of HeLa MCTS after different treatments for 2 d. Scale bar: 50  $\mu$ m. G) Proportion of apoptotic cells in various MCTS groups after 2 d of respective treatments. The data are shown as mean  $\pm$  SD ( $n = 3$ ). H) The inhibitory effect of different treatments on the size growth of HeLa MCTS in 8 d ( $n = 4$ ).  $p$  values:  $**p < 0.01$  or  $*p < 0.05$ . I) A representative MCTS for size measurement; scale bar: 50  $\mu$ m.

monitoring. DOX, either free or in the form of D@RBCs, was applied to the MCTS (diameter  $\approx 400 \mu$ m) on Day 0; and EF treatment for 20 min was applied to the MCTS 12 h later. TUNEL assay was carried out on Day 3. The DAPI staining (blue) of the cell nucleus showed the size of the MCTS, and TUNEL staining identified the cells undergoing apoptosis (with fragmental DNA, green) inside the MCTS. As shown in Figure 4F, the MCTS in the D@RBC and D@RBC+EF groups were much smaller than the other groups, suggesting that the RBC based DDS can effectively prohibit the tumor spheres from growing. TUNEL assay demonstrated that the MCTS in the RBC+EF group had no cancer cell going apoptosis, just as the untreated control. The other four groups all showed certain

positive stained apoptotic cells. Among them, the D@RBC+EF group had the highest anti-tumor efficacy. The proportion of apoptotic cells in the respective MCTS was counted and calculated as shown in Figure 4G. High proportion of apoptotic cells up to 41.4% was detected in the D@RBC+EF group, while in the D@RBC, free DOX, and DOX+EF groups, the apoptotic cells were all around 15%.

The long-term MCTS growth was also monitored by measuring the diameters of the MCTS each other day in 8 d (Figure 4H). The MCTS in the control and RBC groups grew rapidly and continuously. After 8 d, the size of the MCTS enlarged to about 500% in both groups. Meanwhile, the free DOX group had the MCTS size increased to about 300%, and

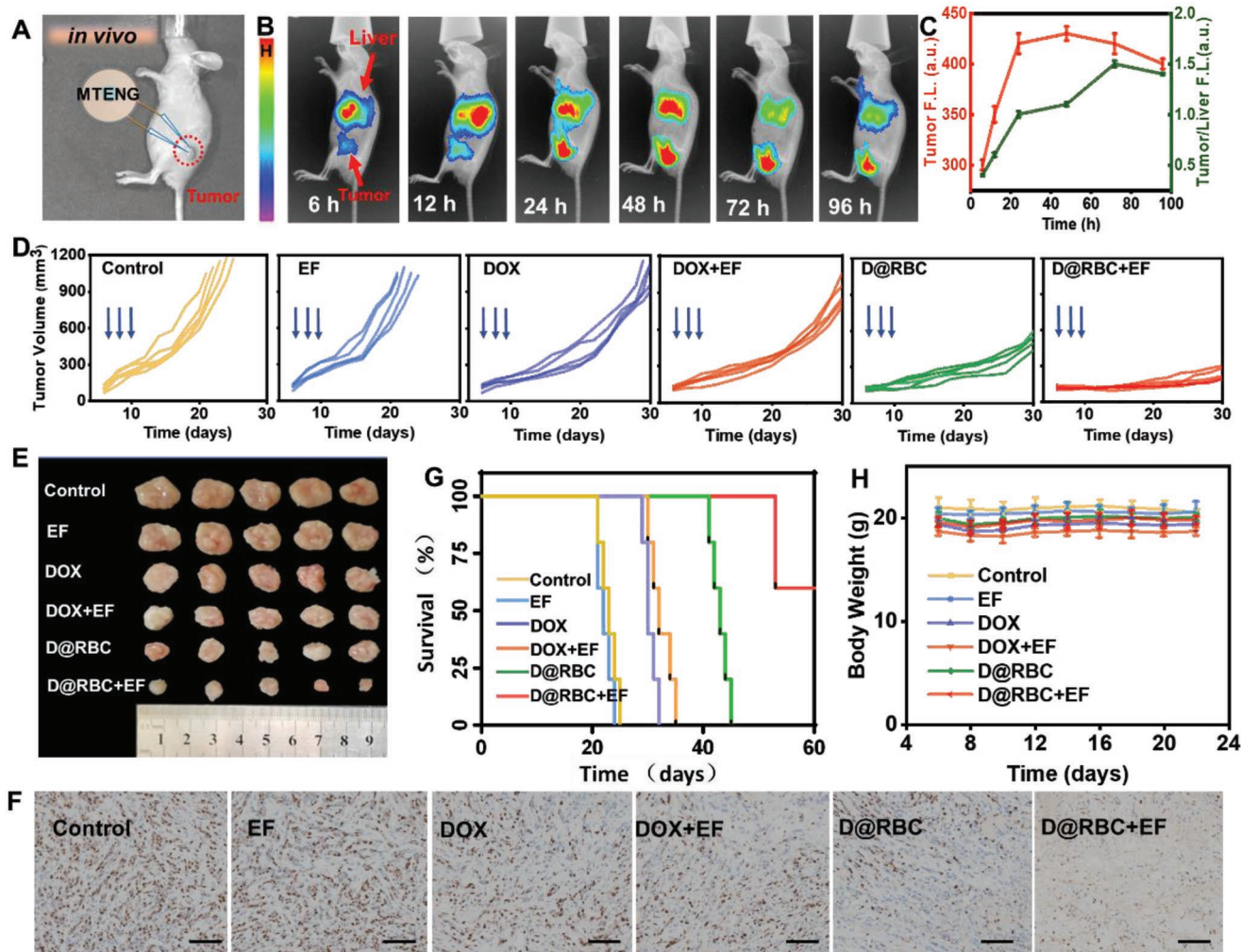


**Figure 5.** MTENG-controlled RBC DDS in vivo. A) The sketch map of MTENG-controlled RBC DDS in the tumor-bearing nude mice. B) Blood circulation and accumulation to tumors of the D@RBCs obtained by in vivo imaging system at 6, 12, 24, 48, 72, and 96 h, respectively. C) The tumor fluorescence intensity and the ratio of tumor-to-liver fluorescence intensity. D) The in vivo tumor growth curve; blue arrows indicate the treatment time point: Day 6, Day 8, and Day 10. E) Image of the harvested tumors in various groups after 1 month. F) The Ki67 immunohistochemistry images of the tumors in various groups (scale bar: 200  $\mu\text{m}$ ). G) The survival curves of the mice in various groups. H) Body weight of the mice.

the DOX+EF and D@RBC groups had the MCTS size increased to about 200%. Contrarily, the MCTS in the D@RBC+EF group stopped growing at the very beginning, demonstrating the most satisfactory inhibition ability. A typical MCTS under the bright field observation for size measurement is shown in Figure 4I.

## 2.6. MTENG-Controlled RBC DDS to Treat Tumors In Vivo

The anti-tumor efficiency of the MTENG-controlled D@RBC DDS was further investigated in vivo in HeLa-tumor-bearing BALB/c-nu mice. The sketch map is shown in Figure 5A. EF generated by the MTENG was delivered to the tumor using the same steel microneedles as used in the MCTS experiment. Before applying various treatments, the distribution of the D@RBCs in the nude mice after inoculation was monitored using the in vivo imaging system (Figure 5B). At 6 h after inoculation, most of the D@RBCs accumulated at the

liver and some of them reached the tumor site. At 48 h after inoculation, the number of D@RBCs locating at the tumor site was almost equal to that at the liver. At 72 h after inoculation, the DOX signal at the liver site declined significantly while the DOX signal at the tumor site decreased only slightly. The tumor fluorescence intensity and the ratio of tumor-to-liver fluorescence intensity are shown in Figure 5C. These results demonstrated the EPR effect of D@RBCs in the tumor-bearing mice. Next, 60 nude mice were randomly divided into six groups, and received HeLa cell inoculation on Day 0. Then they were treated with phosphate buffer saline (PBS), EF, DOX, DOX+EF, D@RBCs, and D@RBC+EF (dose: DOX 5 mg kg<sup>-1</sup>) for three times on Day 6, Day 8, and Day 10, respectively. The tumor size of all groups was measured every 2 d (Figure 5D). For PBS and EF group, the tumor volume showed a rapid and uncontrolled growth pattern. With DOX injected, moderate growth inhibition was observed in the HeLa tumors, indicating that chemotherapy could not completely eliminate the tumor.

The tumor treated with DOX plus EF had almost equal inhibition on the tumor growth as compared to the DOX only group. When mice were treated with D@RBCs, the tumor growth was reduced remarkably due to the accumulated D@RBCs in tumors resulting from the EPR effect. Most importantly, combined with TENG stimulation, D@RBC+EF group showed the most effective tumor growth suppression. The tumors were kept from growing any larger before Day 20; after that they started to grow very slowly. On Day 30, half of the mice in each group were sacrificed and the tumors were harvested as shown in Figure 5E. Tumors in the D@RBC+EF group had significantly smaller volume than the other groups. Meanwhile, Ki67 immunohistochemistry images showed that the D@RBC+EF group had the minimum cell proliferation in the tumors (Figure 5F). The mice survival rate curves are shown in Figure 5G. The mice in the control group started to die from Day 22, and all the mice in the groups other than D@RBC+EF died within 46 d. However, only two out of the five mice in the D@RBC+EF group died on Day 54. The body weight of the mice kept almost unchanged in 22 d, suggesting that the treatment did not cause side effects to the mice (Figure 5H). These results confirmed the outstanding therapeutic efficacy of D@RBC+EF in vivo.

## 2.7. Discussion

Chemotherapeutic drugs lead to severe side effects on healthy cells, including bone marrow, skin, and gastrointestinal mucosa, because they act on all rapidly proliferating cells by inhibiting DNA synthesis and interfering with cell division and metabolism. In this regard, DDS are developed. Briefly, DDS should be able to reach and penetrate to the inside of tumors to function. Moreover, they should have controllable release at the optimal location and time. RBCs are one of the most popular drug delivery vehicles, and EF has long been proved to induce release from the membranes. However, it is difficult to apply EF-controlled RBC DDS in vivo, because the big volume of the electrical supply hinders their clinical applications. Also, many tumors are deep inside the body, it is difficult to deliver EF to those tumors from the outside.

In this work, we successfully developed a self-powered magnet TENG—the MTENG—to enable the EF-controlled RBC based DDS. The MTENG can effectively guarantee the contact and detach cycle between the two friction layers after encapsulation and implantation, to offer a high and consistent electricity output in long terms. The output of the MTENG has been demonstrated to successfully increase the DOX release from RBCs, to dominantly inhibit cancer cells and tumor growth both in vitro and in vivo. These results certified the outstanding performance of MTENG to control the drug release from RBCs and enhance the anti-tumor process.

We particularly investigated the feasibility of using the MTENG to assist the anti-tumor therapy in vivo. Indeed we have to insert the microneedle electrodes into the tumor site to collaborate with DOX@RBCs and achieve the therapeutic effect. This may require a surgery, which seems to be “carrying coals to Newcastle” because a surgery could have removed the tumor already. However, tumors are very complicated diseases,

and in many cases the electrical field based therapy can make great contributions to tumor treatment. For cancers such as nasopharynx carcinoma,<sup>[20]</sup> pancreatic carcinoma,<sup>[21]</sup> and tonsil carcinoma,<sup>[22]</sup> tumors are hard to be removed by surgery due to the lesion location and unknown tumor boundary. Besides, terminal cancer patients often have anemia, dehydration, and metabolic disorders,<sup>[23]</sup> and cannot bear the burden of a resection surgery or radiotherapeutics. In these cases, minimally invasive surgery to implant microneedle electrodes and our miniaturized MTENG is an optimum option. For skin and epidermal cancers, such as melanoma,<sup>[24]</sup> advanced basal cell carcinoma,<sup>[25]</sup> and squamous cell carcinoma,<sup>[26]</sup> patients are prone to have disease recurrence and tumor metastasis following surgery, leading to poor long-term outcomes and relative low survival rate.<sup>[27]</sup> In this regard, we can apply our treatment system as wearable devices without the need of a surgery. We can just insert the tiny tips of electrodes to the superficial tumor with negligible trauma, and electric field can be delivered to the tips through the leads by simply patting the MTENG as a wearable miniaturized power source.

Therefore, our MTENGs are very promising to be applied in the clinic to enable the EF-controlled DDS for tumors. As introduced above, the MTENG can serve as the implantable power source to trigger the drug release in the RBC DDS with rational control. The MTENG can be implanted subcutaneously at the chest area to be self-powered by the body breath. It could also be controlled by external forces applied on the skin. With MTENG serving as the power source and the microneedles serving as the electrodes, the integrated power and stimuli system can be wholly implanted in vivo to provide EF for the controllable DDS to tumors deep inside the body. This will greatly enhance the anti-tumor efficiency while decreasing drug dosage, achieving a satisfactory therapeutic effect for tumors.

## 3. Conclusion

In this work, we have successfully established a self-powered EF-controlled DDS for cancer therapy. The MTENG can effectively guarantee the contact and detach cycle between the two friction layers after encapsulation and implantation, to certify a high and consistent electricity output in long terms. The self-release of DOX from RBCs was very slow. But the EF stimulation generated by the MTENG enabled a much quicker release of DOX. After EF withdrawal, the increased release would also stop, resulting in a controllable release pattern. The EF enhanced DOX@RBC release leads to significantly enhanced killing efficiency of cancer cells both in vitro and in vivo at a low drug dosage. These results have demonstrated a distinguished therapeutic effect with the EF-controlled DDS for cancer therapy. This system is highly promising to be applied in the clinic.

## 4. Experimental Section

*Fabrication of the MTENG:* The fabrication of nude TENG is based on the vertical contact–separation mode. PTFE membrane with nanostructure on the surface and titanium sheet were used as triboelectric layers. The nanopillar structure on the surface of PTFE was fabricated using



inductively coupled plasma (ICP) reactive ion etching. In the etching process, an Au film with the thickness of about 10 nm as a mask was magnetron sputtered on the PTFE surface. A mixed gas of O<sub>2</sub>, Ar, and CF<sub>4</sub> with the corresponding flow rates of 10.0, 15.0, and 30 sccm was used in the ICP chamber. The nanopillars on the PTFE film were produced under the power source of 400 W. After that a Cu film with the thick of nearly 200 nm was deposited on the back of PTFE by magnetron sputtering as electrode. Two magnets were fixed on the back of PTFE film and titanium sheet to separate the triboelectric layers. After the two friction layers fixed by Kapton tape, the nude TENG was first encapsulated by PTFE tape and then by PDMS using spin-coating method. Then the PDMS was solidified at 80 °C for an hour, and cut to a proper size. The electric characterizations were obtained using a Keithley 6514 system electrometer and an SR570 current amplifier from Stanford Research Systems.

**Preparation of D@RBCs:** The DOX was loaded into RBCs using a classical hypotonic method.<sup>[28]</sup> Whole blood was obtained from the eye sockets of Kunming mice. The RBCs were separated from the whole blood by centrifugation (3000 rpm, 5 min). After washed three times with cold PBS (300 mOsm, PH 7.4), the RBCs were re-suspended in PBS (70% hematocrit). About 1 mL hypotonic buffer containing 200 µg mL<sup>-1</sup> DOX, 2 × 10<sup>-3</sup> M ATP, and 3 × 10<sup>-3</sup> M reduced GSH, 10 × 10<sup>-3</sup> M NaH<sub>2</sub>PO<sub>3</sub>, 10 × 10<sup>-3</sup> M NaHCO<sub>3</sub>, 20 × 10<sup>-3</sup> M glucose, and 4 × 10<sup>-3</sup> M MgCl<sub>2</sub> was added to 200 µL RBC suspension slowly. The hypotonic loading process was carried out at 4 °C for 40 min. After centrifugation (3000 rpm, 5 min), the resealing process was carried out. The RBC pellet was re-suspended in a hypertonic solution containing 10% pyruvate-inosine-glucose-NaH<sub>2</sub>PO<sub>4</sub>-adenin (PIGPA)-NaCl (including 2 × 10<sup>-3</sup> M ATP, and 3 × 10<sup>-3</sup> M GSH, 100 × 10<sup>-3</sup> M natrium pyruvate, 100 × 10<sup>-3</sup> M inosine, 100 × 10<sup>-3</sup> M glucose, 35 × 10<sup>-3</sup> M NaH<sub>2</sub>PO<sub>4</sub>, 5 × 10<sup>-3</sup> M adenine, and 12% w/v NaCl) at 37 °C for 40 min. The redundant DOX was removed by washing the RBS with cold PBS (1X, PH 7.4) for four times.

**Characterization of DOX Loaded RBCs:** Confocal fluorescence images were obtained by a Leica SP8 laser scanning confocal microscope. For flow cytometry measurement, the RBCs were analyzed using a cytoflex LX flow cytometer (Beckman). To determine the loading capacity of the DOX, a quantitative DOX uptake assay was conducted by destructing the RBC membranes completely using a lysis buffer and then extracting the released DOX in the solution using a solvent of HCl/isopropanol. DOX was collected from the supernatant solution after centrifugation at 8000 rpm for 5 min and measured using fluorescence spectra. For scanning electron microscopy characterization, the RBCs were collected by centrifugation (3000 rpm, 5 min) and incubated in electron microscopy grade glutaraldehyde (0.25% w/w made in PBS) for 18 h. The cells were isolated by centrifugation (3000 rpm for 5 min) at room temperature and the supernatant was discarded. The dehydration process was conducted by sequentially treating the RBCs with ethanol solutions of increasing concentration (50%, 70%, 80%, 90% v/v and absolute ethanol). RBCs were re-suspended in pure ethanol and placed onto silicon wafer. Gold deposition was performed for 30 s before finally observed using scanning electron microscopy (SU-8020).

**Preparation of the 2D Stimulation Device:** Photoresist (SUN-115 P) was flooded on a cleaned quartz glass at 2500 rpm for 25 s, soft baked for 1 min at 95 °C, and then exposed through a high-resolution transparency mask containing an insert pattern for 15 s. After exposure, the quartz glass was baked at 95 °C for 1 min and developed with photoresist developer for 15 s. A Cu film with a thickness of 200 nm was deposited on the surface of quartz glass by magnetron sputtering as electrode. After removing excess Cu using stripping liquid, the interdigital electrodes were formed. Then a thin PDMS film was spin-coated on the quartz glass and solidified at 80 °C for 1 h. Finally, a biocompatible PLA mold that was prepared by 3D printer was fixed on the top of PDMS film.

**Cells and MCTS Culture:** HeLa cells were cultured in Dulbecco's modified Eagle's medium (DMEM) supplemented with 10% v/v fetal bovine serum (FBS), penicillin (100 U mL<sup>-1</sup>), and streptomycin (100 g mL<sup>-1</sup>) in a humidified incubator at the atmosphere of 37 °C and 5% CO<sub>2</sub>. For preparing 3D MCTS, about 2500 trypsin-dispersed HeLa cells were seeded into agarose (Sigma-Aldrich, Shanghai, China) precoated 96-well

plates (Sigma-Aldrich) in DMEM media (200 µL).<sup>[29]</sup> MCTS were let to grow for 4 d of stationary culture until they finally reached a diameter of 400 µm, which were ready to receive the EF and RBC treatments.

**D@RBC Penetration into 3D MCTS:** For the convenience of observation under fluorescence microscope, the D@RBCs were stained by 1,1'-dioctadecyl-3,3,3',3'-tetramethylindocarbocyanine perchlorate (DiD) dye for 20 min. After that MCTS was co-cultured with 1 µL D@RBCs for 12 h. Then the free D@RBC was washed away by PBS for three times. Images were acquired by an Olympus IX 71 fluorescence microscope.

**Preparation of 3D Stimulation Device:** Commercial medical steel microneedles with a tip diameter of 100 µm were used for EF stimulation in the experiment. The tips of the microneedles were encapsulated by parylene C and the needles were connected to a larger MTENG with the output of about 300 V. One pair of the needles was inserted in the 96-well plate for stimulation, and the gap between the two needles was about 400 µm.

**TUNEL Assay and Growth Monitor for MCTS:** DOX (1 µg mL<sup>-1</sup>), either free or in the form of D@RBCs, was applied to the MCTS (diameter ≈400 µm) on Day 0; and EF treatment for 20 min was applied to the MCTS 12 h later. TUNEL assay was carried out on Day 3 using the in situ cell death detection kit (Merck Millipore, Darmstadt, Germany). For the inhibition experiment of MCTS, the culture media was half replaced every time. Images of spheroids were captured using a bright light microscope with a 10 × objective lens connected to a digital camera. Spheroid size was determined by measuring their diameters (*d*). The volume of the MCTS was calculated as follows:  $V = 4/3 \times \pi \times (d/2)^3$ . The data were processed as the mean volume ± SD (*n* = 4).

**In Vivo HeLa Tumor-Bearing Mice Model:** The experimental animals (BALB/c nude mice, female, 4–6 weeks old) were purchased from the Vital River Laboratory Animal Technology Co. Ltd. (Beijing, China). The mice were maintained in a pathogen-free environment and allowed to acclimate for 1 week before tumor implantation. About 6 × 10<sup>6</sup> HeLa cells (in 100 µL 1X PBS) were inoculated subcutaneously into the left side of the mice's backs to develop xenograft tumors. After about 1 week, the volume of the tumors reached about 100 mm<sup>3</sup>.

**Blood Circulation and In Vivo Tumor Accumulation of D@RBCs:** D@RBCs were treated ultrasonically for 5 min during DOX loading in the in vivo study. Then they were stained by DiD, and intravenously injected to HeLa tumor-bearing mice at the DOX dose of 5 mg kg<sup>-1</sup> body weight. At 6, 12, 24, 48, 72, and 96 h, respectively, the tissue distribution was imaged by the In Vivo imaging system (FX Pro, Kodak).

**In Vivo Anti-Tumor Evaluation:** About 60 tumor-bearing mice were randomly divided into control (PBS), EF (+PBS), DOX, DOX+EF, D@RBC, and D@RBC+EF groups. About 200 µL PBS, DOX, or D@RBC were injected to mice through tail vein, respectively (dose: DOX 5 mg kg<sup>-1</sup>) on Day 6, Day 8, and D10, to give a total administration of three-drug treatment in the experiment. EF stimulation was applied 12 h after the drug inoculation for 20 min each time. Parylene C packaged medical steel microneedles with a tip diameter of 100 µm were used as electrodes for EF stimulation. The microneedle electrodes connected to the MTENG and with a gap of 400 µm at the tips were inserted into the tumor. On Day 30, half of the mice in each group were sacrificed and the tumors were harvested. The digital images of the tumors were taken, and anti-Ki67 immunohistochemical assay was done with the frozen tumor slices. The other half of mice were maintained for survival record.

## Supporting Information

Supporting Information is available from the Wiley Online Library or from the author.

## Acknowledgements

C.C.Z., H.Q.F., and L.J.Z. contributed equally to this work. This work was supported by the National Key R&D Project from the Ministry of

Science and Technology, China (Grant Nos. 2016YFA0202703 and 2017YFA0207900), the National Natural Science Foundation of China (Grant Nos. 61875015, 31571006, 81601629, and 21801019), Beijing Talents Fund (Grant No. 2015000021223ZK21), the Beijing Natural Science Foundation (Grant No. 2182091), and the National Youth Talent Support Program.

## Conflict of Interest

The authors declare no conflict of interest.

## Keywords

cancer therapy, drug delivery, enhanced permeability and retention (EPR) effect, nanogenerator, red blood cells (RBCs)

Received: December 5, 2018

Revised: December 29, 2018

Published online:

- [1] a) A. Garaventa, R. Luksch, S. Biasotti, G. Severi, M. R. Pizzitola, E. Viscardi, A. Prete, S. Mastrangelo, M. Podda, R. Haupt, B. De Bernardi, *Cancer* **2003**, *98*, 2488; b) J. Z. Zhu, J. Zhang, D. Xiang, Z. H. Zhang, L. Zhang, M. Y. Wu, S. Y. Zhu, R. Y. Zhang, W. Han, *Eur. J. Pharmacol.* **2010**, *643*, 247; c) C. Chen, W. Xu, C. M. Wang, *Leuk. Lymphoma* **2013**, *54*, 2517.
- [2] a) E. Calvo, V. Moreno, M. Flynn, E. Holgado, M. E. Olmedo, M. P. L. Criado, C. Kahatt, J. A. Lopez-Vilarino, M. Siguero, C. Fernandez-Teruel, M. Cullerell-Young, A. S. Matos-Pita, M. Forster, *Ann. Oncol.* **2017**, *28*, 2559; b) M. E. Buyukokuroglu, S. Taysi, M. Buyukavci, *Asian J. Chem.* **2007**, *19*, 4035; c) P. Schmid, J. Krockner, C. Jehn, K. Michniewicz, S. Lehenbauer-Dehm, H. Eggemann, V. Heilmann, S. Kummel, C. O. Schulz, A. Dieing, M. B. Wischnewsky, S. Hauptmann, D. Elling, K. Possinger, B. Flath, *Ann. Oncol.* **2005**, *16*, 1624; d) M. E. R. O'Brien, N. Wigler, M. Inbar, R. Rosso, E. Grischke, A. Santoro, R. Catane, D. G. Kieback, P. Tomczak, S. P. Ackland, F. Orlandi, L. Mellars, L. Alland, C. Tendler, C. B. C. S. Grp, *Ann. Oncol.* **2004**, *15*, 440.
- [3] a) C. M. J. Hu, L. Zhang, S. Aryal, C. Cheung, R. H. Fang, L. F. Zhang, *Proc. Natl. Acad. Sci. USA* **2011**, *108*, 10980; b) S. Mura, F. Pirot, M. Manconi, F. Falson, A. M. Fadda, *J. Drug Targeting* **2007**, *15*, 101; c) M. L. Tan, A. M. Friedhuber, D. E. Dunstan, P. F. M. Choong, C. R. Dass, *Biomaterials* **2010**, *31*, 541; d) Z. G. Yue, W. Wei, Z. X. You, Q. Z. Yang, H. Yue, Z. G. Su, G. H. Ma, *Adv. Funct. Mater.* **2011**, *21*, 3446.
- [4] C. Wong, T. Stylianopoulos, J. A. Cui, J. Martin, V. P. Chauhan, W. Jiang, Z. Popovic, R. K. Jain, M. G. Bawendi, D. Fukumura, *Proc. Natl. Acad. Sci. USA* **2011**, *108*, 2426.
- [5] D. Zhao, Q. Chen, H. Song, S. T. Luo, P. Y. Ge, Y. J. Wang, J. Y. Ma, Z. Li, X. M. Gao, X. M. Zhao, X. Subinuer, H. Y. Yang, X. J. Jiang, Y. X. Chen, X. Zhu, *Nanomedicine* **2018**, *13*, 1517.
- [6] K. S. Oh, K. Kim, B. D. Yoon, H. J. Lee, D. Y. Park, E. Y. Kim, K. Lee, J. H. Seo, S. H. Yuk, *Int. J. Nanomed.* **2016**, *11*, 1077.
- [7] S. Kim, R. Diab, O. Joubert, N. Canilho, A. Pasc, *Colloids Surf., B* **2016**, *140*, 161.
- [8] X. J. Zhang, K. Achazi, R. Haag, *Adv. Healthcare Mater.* **2015**, *4*, 585.
- [9] a) Y. L. Lv, M. Liu, Y. Zhang, X. F. Wang, F. Zhang, F. Li, W. E. Bao, J. Wang, Y. L. Zhang, W. Wei, G. H. Ma, L. C. Zhao, Z. Y. Tian, *ACS Nano* **2018**, *12*, 1350; b) K. Xiong, W. Wei, Y. J. Jin, S. M. Wang, D. X. Zhao, S. Wang, X. Y. Gao, C. M. Qiao, H. Yue, G. H. Ma, H. Y. Xie, *Adv. Mater.* **2016**, *28*, 7929; c) L. Rao, L. L. Bu, B. Cai, J. H. Xu, A. Li, W. F. Zhang, Z. J. Sun, S. S. Guo, W. Liu, T. H. Wang, X. Z. Zhao, *Adv. Mater.* **2016**, *28*, 3460.
- [10] a) A. S. Timin, M. M. Litvak, D. A. Gorin, E. N. Atochina-Vasserman, D. N. Atochin, G. B. Sukhorukov, *Adv. Healthcare Mater.* **2018**, *7*, 1700818; b) F. Pierige, S. Serafini, L. Rossi, A. Magnani, *Adv. Drug Delivery Rev.* **2008**, *60*, 286; c) W. W. Gao, C. M. J. Hu, R. H. Fang, B. T. Luk, J. Su, L. F. Zhang, *Adv. Mater.* **2013**, *25*, 3549.
- [11] H. Nehoff, N. N. Parayath, L. Domanovitch, S. Taurin, K. Greish, *Int. J. Nanomed.* **2014**, *9*, 2539.
- [12] a) X. Q. Sun, C. Wang, M. Gao, A. Y. Hu, Z. Liu, *Adv. Funct. Mater.* **2015**, *25*, 2386; b) L. Rao, B. Cai, L. L. Bu, Q. Q. Liao, S. S. Guo, X. Z. Zhao, W. F. Dong, W. Liu, *ACS Nano* **2017**, *11*, 3496.
- [13] a) E. V. Skorb, H. Mohwald, *Adv. Mater. Interfaces* **2014**, *1*, 1400237; b) X. Q. Sun, C. Wang, M. Gao, A. Y. Hu, Z. Liu, *Nanomedicine* **2016**, *12*, 548; c) K. Kinoshita, T. Y. Tsong, *Nature* **1977**, *268*, 438; d) G. T. Yu, L. Rao, H. Wu, L. L. Yang, L. L. Bu, W. W. Deng, L. Wu, X. L. Nan, W. F. Zhang, X. Z. Zhao, W. Liu, Z. J. Sun, *Adv. Funct. Mater.* **2018**, *28*, 1801389.
- [14] a) E. Neumann, S. Kakorin, K. Toensing, *Faraday Discuss.* **1999**, *111*, 111; b) M. L. Yarmush, A. Golberg, G. Sersa, T. Kotnik, D. Miklavcic, *Annu. Rev. Biomed. Eng.* **2014**, *16*, 295.
- [15] a) Z. Li, G. A. Zhu, R. S. Yang, A. C. Wang, Z. L. Wang, *Adv. Mater.* **2010**, *22*, 2534; b) G. J. Zhang, Q. L. Liao, M. Y. Ma, F. F. Gao, Z. Zhang, Z. Kang, Y. Zhang, *Nano Energy* **2018**, *52*, 501; c) U. Khan, T. H. Kim, H. Ryu, W. Seung, S. W. Kim, *Adv. Mater.* **2017**, *29*, 1603544; d) Y. C. Mao, P. Zhao, G. McConohy, H. Yang, Y. X. Tong, X. D. Wang, *Adv. Energy Mater.* **2014**, *4*, 1301624.
- [16] a) H. S. Wang, C. K. Jeong, M. H. Seo, D. J. Joe, J. H. Han, J. B. Yoon, K. J. Lee, *Nano Energy* **2017**, *35*, 415; b) Y. J. Su, X. N. Wen, G. Zhu, J. Yang, J. Chen, P. Bai, Z. M. Wu, Y. D. Jiang, Z. L. Wang, *Nano Energy* **2014**, *9*, 186; c) Y. Qin, X. D. Wang, Z. L. Wang, *Nature* **2008**, *451*, 809.
- [17] a) Q. F. Shi, H. Wang, T. Wang, C. Lee, *Nano Energy* **2016**, *30*, 450; b) G. H. Lim, S. S. Kwak, N. Kwon, T. Kim, H. Kim, S. M. Kim, S. W. Kim, B. Lim, *Nano Energy* **2017**, *42*, 300; c) S. Lee, H. Wang, Q. F. Shi, L. Dhakar, J. H. Wang, N. V. Thakor, S. C. Yen, C. Lee, *Nano Energy* **2017**, *33*, 1; d) H. T. Chen, Y. Song, H. Guo, L. M. Miao, X. X. Chen, Z. M. Su, H. X. Zhang, *Nano Energy* **2018**, *51*, 496.
- [18] a) P. Y. Song, S. Y. Kuang, N. Panwar, G. Yang, D. J. H. Tng, S. C. Tjin, W. J. Ng, M. B. Majid, G. Zhu, K. T. Yong, Z. L. Wang, *Adv. Mater.* **2017**, *29*, 1; b) H. Ouyang, J. J. Tian, G. L. Sun, Y. Zou, Z. Liu, H. Li, L. M. Zhao, B. J. Shi, Y. B. Fan, Y. F. Fan, Z. L. Wang, Z. Li, *Adv. Mater.* **2017**, *29*, 1703456.
- [19] a) Q. Zheng, Y. M. Jin, Z. Liu, H. Ouyang, H. Li, B. J. Shi, W. Jiang, H. Zhang, Z. Li, Z. L. Wang, *ACS Appl. Mater. Interfaces* **2016**, *8*, 26697; b) Q. Zheng, H. Zhang, B. J. Shi, X. Xue, Z. Liu, Y. M. Jin, Y. Ma, Y. Zou, X. X. Wang, Z. An, W. Tang, W. Zhang, F. Yang, Y. Liu, X. L. Lang, Z. Y. Xu, Z. Li, Z. L. Wang, *ACS Nano* **2016**, *10*, 6510.
- [20] M. Frikha, A. Auperin, Y. Tao, F. Elloumi, N. Toumi, P. Blanchard, P. Lang, S. Sun, S. Racadot, J. Thariat, M. Alfonsi, C. Tuchais, A. Cornely, A. Moussa, J. Guigay, J. Daoud, J. Bourhis, GORTEC, *Ann. Oncol.* **2018**, *29*, 731.
- [21] I. K. Komenaka, R. Mir, J. B. de Graft-Johnson, L. Wise, *Lancet Oncol.* **2003**, *4*, 373.
- [22] D. Williamson, J. Anderson, D. Ash, C. Coyle, M. Sen, *Ann. Oncol.* **2006**, *17*, 183.
- [23] a) M. P. Campos, B. J. Hassan, R. Riechelmann, A. Del Giglio, *Ann. Oncol.* **2011**, *22*, 1273; b) A. Alistar, B. B. Morris, R. Desnoyer, H. D. Klepin, K. Hosseinzadeh, C. Clark, A. Cameron, J. Leyendecker, R. D'Agostino Jr., U. Topaloglu, L. W. Boteju, A. R. Boteju, R. Shorr, Z. Zachar, P. M. Bingham, T. Ahmed, S. Crane, R. Shah, J. J. Migliano, T. S. Pardee, L. Miller, G. Hawkins, G. Jin, W. Zhang, B. Pasche, *Lancet Oncol.* **2017**, *18*, 770.
- [24] a) K. J. L. Bell, Y. Mehta, R. M. Turner, R. L. Morton, M. Dieng, R. Saw, P. Guitera, K. McCaffery, D. Low, C. Low, M. Jenkins, L. Irwig,

- A. C. Webster, *Psychooncology* **2017**, *26*, 1784; b) M. A. McKean, R. N. Amaria, *Cancer Treat. Rev.* **2018**, *70*, 144; c) H. Mishra, P. K. Mishra, A. Ekielski, M. Jaggi, Z. Iqbal, S. Talegaonkar, *J. Cancer Res. Clin. Oncol.* **2018**, *144*, 2283.
- [25] a) M. R. Migden, A. L. S. Chang, L. Dirix, A. J. Stratigos, J. T. Lear, *Cancer Treat. Rev.* **2018**, *64*, 1; b) T. C. Watt, P. D. Inskip, K. Stratton, S. A. Smith, S. F. Kry, A. J. Sigurdson, M. Stovall, W. Leisenring, L. L. Robison, A. C. Mertens, *JNCI: J. Natl. Cancer Inst.* **2012**, *104*, 1240.
- [26] J. E. Leeman, J. G. Li, X. Pei, P. Venigalla, Z. S. Zumsteg, E. Katsoulakis, E. Lupovitch, S. M. McBride, C. J. Tsai, J. O. Boyle, B. R. Roman, L. G. T. Morris, L. A. Dunn, E. J. Sherman, N. Y. Lee, N. Riaz, *JAMA Oncol.* **2017**, *3*, 1487.
- [27] a) F. J. H. Hoogwater, N. Snoeren, M. W. Nijkamp, A. C. Gunning, W. J. Van Houdt, M. T. De Bruhn, E. E. Voest, R. Van Hillegersberg, O. Kranenburg, I. H. M. B. Rinkes, *Anticancer Res.* **2011**, *31*, 4507; b) V. Liska, L. Holubec, V. Treska, T. Skalicky, A. Sutnar, S. Kormunda, J. Finek, O. Topolcan, *Anticancer Res.* **2008**, *28*, 3387.
- [28] C. G. Millan, A. Z. Castaneda, M. L. S. Marinero, J. M. Lanao, *Blood Cells Mol. Dis.* **2004**, *33*, 132.
- [29] J. Friedrich, C. Seidel, R. Ebner, L. A. Kunz-Schughart, *Nat. Protoc.* **2009**, *4*, 309.